Spin-wave propagation in α-Fe_2O_3 nanorods: The effect of confinement and disorder

David Cortie[1,*], Gilberto Casillas-Garcia[2], Andrew Squires[3], Richard Mole[4], Xiaolin Wang[1], Yun Liu[5], Yen-Hua Chen [6,†] and Dehong Yu[4]

[1] ARC Centre of Excellence in Future Low-Energy Electronics Technologies (FLEET), The Institute for Superconducting and Electronic Materials, The University of Wollongong, New South Wales 2500, Australia
[2] Electron Microscopy Centre, Australian Institute of Innovative Materials, The University of Wollongong, New South Wales 2522, Australia
[3] School of Physics, Faculty of Engineering and Information Sciences, University of Wollongong, New South Wales 2522, Australia
[4] The Australian Nuclear Science and Technology Organisation, Lucas Heights, NSW 2232, Australia
[5] The Research School of Chemistry, The Australian National University, ACT 2601, Australia
[6] Department of Earth Sciences, National Cheng Kung University, 1, University Rd., East Dist., Tainan City 701, Taiwan, ROC

* Correpsonding Authors' e-mail: dcortie@uow.edu.au † yhc513@mail.ncku.edu.tw

Abstract

Spin-wave excitations in α-Fe_2O_3 nanorods were directly detected using time-of-flight inelastic neutron spectroscopy. The dispersive magnon features are compared with those in bulk α-Fe_2O_3 particles at various temperatures to highlight differences in mode intensity and width. The interchanged spectral intensities in the nanorod are a consequence of a suppressed spin orientation, and this is also evident in the neutron diffraction which demonstates that the weak ferromagnetic phase survives to 1.5 K. Transmission electron microscopy shows that the ellipsoidal particles are single-crystalline with a typical length of 300 ± 100 nm and diameter of 60 ± 10 nm. The main magnon features are similar in bulk and nanoforms and can be explained using a model Hamiltonian based on Samuelson and Shirane's classical theory with exchange constants of J_1=-1.03 meV, J_2= -0.28 meV, J_3= 5.12 meV and J_4=4.00 meV. Numerical simulations show that two distinct mechanisms may contribute to the magnon line broadening in the nanorods: a distribution of exchange interactions caused by disorder, and a shortened quasiparticle lifetime caused by the scattering of spin waves at surfaces.

Keywords: geomagnetism, spintronics, magnonics, magnetic oxides

1. Introduction

Throughout history, the mineral hematite (α-Fe_2O_3) has left an indelible mark as its blood-red color has been a popular component in paints used on ancient cave walls through to modern artworks. While the optical functionality is evident to the naked eye, the magnetic properties of α-Fe_2O_3 remained virtually unknown until the middle of the 20th century. This is because the atomic-scale antiferromagnetic structure in α-Fe_2O_3 produces a negligible macroscopic moment which is difficult to detect directly using magnetic attraction [1]. Consequently, the details of the spin structure in α-Fe_2O_3 remained unknown until the development of experimental neutron diffraction techniques. Even today, the vanishingly small magnetization ensures that bulk hematite has no known magnetic applications. In the past decade, however, nanoscale forms of α-Fe_2O_3 have received intensive attention for potential applications in spintronics and low energy electronics, including as pinning layers for spin-valve systems [2] [3, 4] and, as a way to transmit pure magnon currents over long distances [5] which is prerequisite for a new class of spin transistor [6]. Recently, ultra-thin α-Fe_2O_3 has been theoretically proposed as a platform for achieving the Quantum Anomalous Hall effect [7]. Despite these advances, many properties of nanoscale and few-layer α-Fe_2O_3 remain enigmatic. This article presents new experimental evidence for the magnetic structure and spin-wave propagation in rod-like particles of α-Fe_2O_3.

Although α-Fe_2O_3 is one of the oldest and most heavily studied bulk antiferromagnets, it shows unexplained behaviors near

surfaces and in nanoscale particles. For example, the spin reorientation transition (SR) occurs at T_{SR} =260 K in bulk α-Fe_2O_3 and this known as the Morin point [1]. In nanostructures such as particles, rods, cones, and films, the Morin transition is anomalous and can occur over a wide range of conditions between 2 K and 400 K, or even vanish altogether. The first-order SR transition in nanohematite is reported to depend on factors including size [8], stoichiometry [9], strain [10], water content [11] and magnetic surface anisotropy [12]. The exact role of each of the aforementioned factors has never been unambigously established. From a geological perspective, the relationship between particle morphology and the magnetism in nanostructures of hematite is important, since natural nanoparticles of this oxide are chemically stable and ubiquitous on Earth and Mars where they influence geomagnetic and chemical processes in the environment. As a strongly electron-correlated oxide, the electronic structure, chemical structure and magnetism of hematite are entangled, and cannot be understood in isolation from one another. Thus the shape of nanocrystallites and their magnetic behavior is both an important environmental indicator, and also a factor in surprising properties such as the giant magnetic exchange bias discovered in natural ores [13]. From the spintronics perspective, the robust feature that makes α-Fe_2O_3 potentially attractive is the high intrinsic Néel temperature (955 ± 10 K) [1]. Even in small nanostructures and monolayers, where finite-size effects do moderately reduce the transition [14], magnetic order invariably survives to room temperature [15, 16]. However, it remains critical to understand the modifications to the spin reorientation that occur near surfaces, and in nanostructures, because this determines nearly all of the functional properties from the magnetic exchange bias [3] to whether time-reversal symmetry is broken in order to influence topological magnetic states [7]. Currently, there are no convincing general theories that account for the role of size, shape, strain and surface facets in nanostructured and ultrathin α-Fe_2O_3.

Decades of Mössbauer and magnetometry studies on α-Fe_2O_3 nanoparticles have shown that the spin reorientation is shifted to lower temperatures [8, 11] [17] [18], and particles can remain trapped in the weak ferromagnetic state down to the lowest measuring temperatures (2-5 K) [19]. The shape of the majority of the particles studied is spherical or cubic [17]. From reviewing the literature on equiaxial particles, it can be shown that the spin reorientation temperature (T_{SR}) phenomenalogically obeys the relationship: [20]:

$$\frac{T_{SR}}{T_0} = 1 - \left(\frac{L_0}{L_{SR}}\right)^{1/v} \quad (1)$$

where L_{SR} is the diameter of the particle, T_0 is the bulk Morin temperature (260 K), and the characteristic confinement lengthscale is L_0 = 11 nm with the anomalous finite size 'critical exponent' $v \sim 1.0$. Within this model, if a particle length-scale is less than 11 nm, T_{SR} is decreased below zero, whereas for a length-scale of 40 nm, the Morin transition should occur at 189 Kelvin. Neutron diffraction and spectroscopy studies have also been conducted on α-Fe_2O_3 particles for sizes 8-15 nm, and have indeed shown that Morin transition does not occur, at least down to 2 K [21]. A clue to the physical mechanism for the modified spin reorientation was given by the first neutron spectroscopy studies which showed that the spin-wave spectrum in spherical particles (d < 20 nm) is altered [22, 23]. This produces two new resonant features near the magnon band-edge, whereas the 'dispersive' modes from the long-range travelling excitations known from bulk hematite appeared to be absent below 20 meV [21]. As soft-surface magnons are theoretically proposed to mediate the Morin transition, the differences in the nanoparticle spectrum are significant [23]. In particular, the spin gap is quite different from that of bulk hematite, showing a different temperature dependency [22]. A more recent study has also reported the weak signals corresponding to long range dispersion co-existing with the strong resonant features in spherical 15 nm particles [24].

Whereas equiaxial particles have been heavily investigated, fewer studies have investigated the magnetic structure of more complex nanoarchitectures and α-Fe_2O_3 surfaces. Mesoporous α-Fe_2O_3 was investigated by neutron spectroscopy [24] and neutron diffraction [25], and long-range magnon dispersion was observed, in close analogy to bulk hematite. Magnetometry studies have been conducted on α-Fe_2O_3 nanorods, and it was found that ellipsoidal rods do not spin reorientate, whereas highly-faceted rectangular rods do spin reorientate [26]. On this basis, it was argued that surface effects are important. This is consistent with past Mössbauer studies on α-Fe_2O_3 surfaces which detected suppressed hyperfine fields near the surface either in small particles with surfaces labelled with Fe^{57} [15] or in single-crystalline surfaces studied with conversion techniques [27] [28]. Most recently, low energy β-NMR spectroscopy, which is a technique closely related to μSR, detected the modifed nuclear relaxation rate of Li defects implanted near the (110) surface of bulk single crystal α-Fe_2O_3, which is further evidence of an intrinsic surface anisotropy [20]. A consequence of this built-in surface anisotropy is that α-Fe_2O_3 should display a dependency not just on finite size but also on shape, based on proximity to specific crystal facets in nanostructures. The following sections in this Article examine the manifestation of these effects in the spin-wave spectrum of α-Fe_2O_3 nanorods.

2. Methods

1.1 Synthesis

The hematite nanorods were synthesized at the National Cheng Kung University using a hydrothermal method, identical to that reported previously [16]. To summarise, 0.02 M $FeCl_3$ and 7.4×10^{-4} M $NH_4H_2PO_4$ were mixed in a beaker and stirred for 15 min. The solution mixture was then placed in an autoclave heated at 220°C for 6 hours and subsequently allowed to cool to room temperature. The precipitates were separated from the mother liquor by centrifugation and washed using deionized water. Subsequently, the precipitates were dried at 60°C for 6 hours, yielding hematite nanorods. The synthesis procedures were repeated five times to yield sufficient mass for the neutron experiment. To provide a control sample, bulk α-Fe_2O_3 was purchased from Sigma Aldrich and used for comparison. The crystal structure of hematite nano-rod was characterized using a Bruker, D8 Advance X-ray powder diffractometer (Co Kα λ =1.789 Å). The FullProf suite was used for refinement[29]. Magnetic measurements were performed on a Quantum Design PPMS using a Vibrating Sample Magnetometer.

1.2 Neutron scattering

Inelastic neutron spectroscopy experiments were conducted on the PELICAN time-of-flight (TOF) neutron spectrometer at the Australian Centre for Neutron Scattering (ACNS) [30]. The α-Fe_2O_3 powder sample was placed in an annular aluminium sample can. The sample was heated for 4 hours at 135 ºC in a vacuum furnace to remove residual water which otherwise led to a strong quasi-elastic background signal. After water removal, the sample was attached to the cold head of a closed-cycle refrigerator. The instrument was optimised for scans at 4.69 Å neutrons affording an energy resolution approximated by a Gaussian full-width-at-half-maximum (FWHM) of 135 μeV at the elastic line. To account accurately for the slight *Q*-dependence (angular dependence) of resolution function, all data in the low energy region were fitted by convolving the data with the true resolution function determined by measuring a vanadium standard. The data on the area detector was also normalised to the signal from the vanadium standard to correct the per-pixel efficiency. The background signal was subtracted using scans of an empty sample can under identical conditions. Data were transformed into $S(Q,\omega)$ for direct visualization. Data manipulations and fitting were carried out using the Large Array Manipulation Program (LAMP) [31]. Fitting was performed using custom-written procedures in IgorPro.

1.3 Scanning transmission electron microscopy

Transmission electron microscopy (TEM) and scanning transmission electron microscopy (STEM) was performed on a JEOL 200F operating at 200 keV, based at the Electron Microscopy Centre at the University of Wollongong. High-Angle, Annular Dark Field (HAADF) and bright-field images were obtained at atomic-scale resolution, together with electron energy loss spectroscopy (EELS).

1.4 Theoretical calculations

Calculations of the spin-wave dispersion were performed using a semiclassical method employing the SpinW software based on linear spin-wave theory [32]. The minimal model Hamiltonian was:

$$\mathcal{H} = \sum_{i,j} \boldsymbol{S}_i J_{ij} \boldsymbol{S}_j \quad (2)$$

The main term represents the magnetic exchange interactions through Fe-O-Fe super-exchange bonds with a coupling strength of J_{ij}, where the spin on each Fe is represented by S_i, and the sum is performed up to fourth nearest neighbours. Initial estimates for the exchange constants J_{ij} for the first (J_1), second (J_2), third (J_2) and fourth (J_2) set of neighbours were taken from [33]. More complex terms including the Dzyaloshinskii-Moriya interaction (DMI) and the single ion anisotropy (SIA) term are well-known to affect the susceptibility of α-Fe_2O_3 at the low energy scale. However, past work has shown that the meV-scale spin-waves in α-Fe_2O_3 are dominated by the strong exchange interactions (J_{ij}) given that the DMI interactions and SIA are 2-3 orders of magnitude smaller [1, 33]. It is thus justifiable to omit the latter in order to avoid over-parametrization of the problem. In Appendix A, however, additional calculations are presented including the DMI and SIA terms which show that, for any realistic values, these do not modify the spin wave dispersion in the experimental energy range as probed by the PELICAN. Additional high energy neutron spectroscopy data up to 100 meV was digitized from [33] for comparison. The FullPROF software suite was used to calculate the magnetic powder diffraction patterns obtained in the elastic channel of the TOF experiment. The VESTA software was used for visualizing the structure [34].

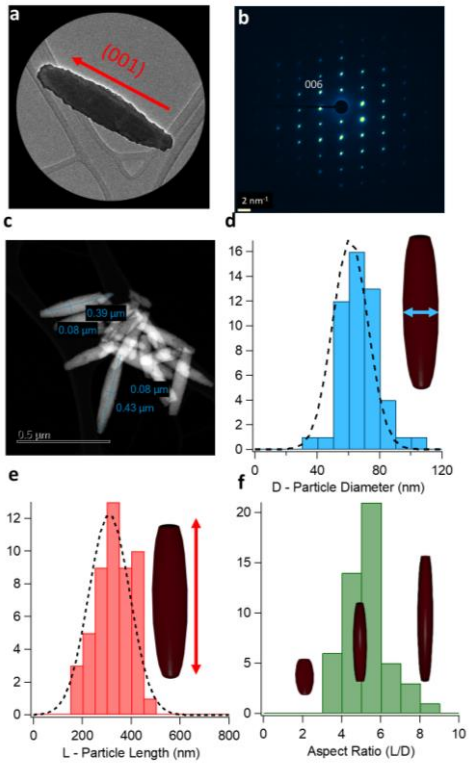

Figure 1.a) The α-Fe_2O_3 nanorods have an ellipsoidal shape as evident in the transmission electron microscopy. b) Single crystalline electron diffraction patterns are observed for the rods, and no obvious twinning can be detected. c) A distribution of particle sizes is observed in the powder ensemble, d) From particle analysis, the average shorter dimension $\langle D \rangle$= 60 nm. e) The average length $\langle L \rangle$ of the particle is 300 nm. f) The aspect ratio $\langle D/L \rangle$ of the majority of individual particles is between 4 and 6.

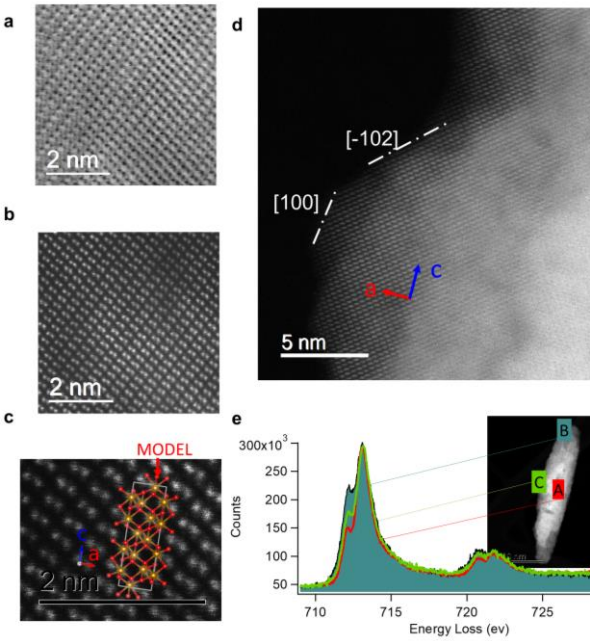

Figure 2.a) Bright-field atomic-scale scanning transmission electron microscopy of a region in the nanorod. b) High angle angular dark field (HAADF) images of the same region. c) Enlarged HAADF region showing the position of the Fe atoms in an orientated hexagonal hematite unit cell superimposed in a (0-10) projection. d) High resolution image of the facets at the serrated edge of the rod identifying two major crystal surfaces. e) Electron energy loss spectrum collected for 3 distinct regions of a nanorod showing a chemical shift consistent with Fe^{3+}.

3. Results and Discussion

The α-Fe_2O_3 particles form elongated ellipsoidal rods with a flat top, as observed in the TEM microscopy (Figure 1 a). The particles are single crystalline as evident in their selected-area electron diffraction patterns (Figure 1 b) which are collected for region containing a single rod as shown Figure 1 a. This indicates the long axes of the rods are orientated along the hexagonal c-direction (001) of the α-Fe_2O_3. These results are consistent with past reports using similar synthesis methods [26]. The rod surface morphology is rough and serrated, implying a mixture of crystal facets. There is a distribution of sizes, however the geometrical features are broadly similar (Figure 1 c). By analysing 50 particles, the mean length of $\langle L \rangle$ = 300 nm and a mean diameter of $\langle D \rangle$ = 60 nm were determined (Figure 1 d-e). There is a spread of aspect ratios for individual rods between 3 and 8 as shown in Figure 1 f.

The crystallinity of the nanorods at the atomic scale can be clearly observed in the scanning TEM images in bright field (Figure 2 a) and in dark field mode (Figure 2b). Several rods were examined and display consistent features, confirming the hexagonal c-axis direction pointing along the elongated axis, which is equivalent to the $(111)^R$ direction in rhombohedral notation. A distinctive doublet-spot feature is evident in the high angular dark field (HAADF) images (Figure 2b). Whereas bright-field images include diffraction contrast, the HAADF images are directly sensitive to the position of the heavy elements (i.e Fe). A structural model of a single unit cell of α-Fe_2O_3, in hexagonal representation, is overlaid upon the enlarged region in Figure 2 c) and good agreement is found with HAADF image along the (0-10) projection. Hematite is characterized by a short and a long Fe-Fe distance along (001) hexagonal direction. This is measured from HAADF line profiles, giving the spacing as 2.9 ± 0.1 Å and 3.8 ± 0.1 Å

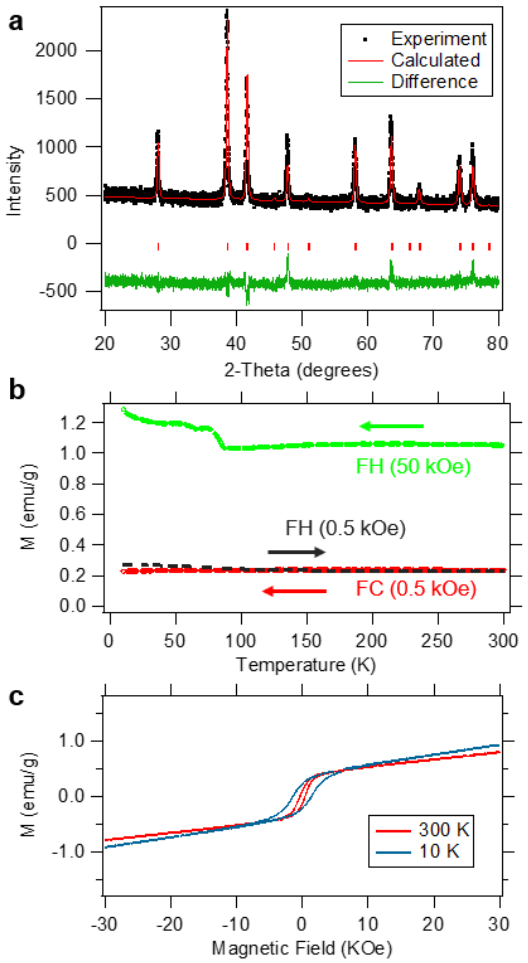

Figure 3. a) X-ray diffraction pattern and Rietveld refinement of the α-Fe_2O_3 nanorods. b) Magnetization versus temperature of the nanorods. c) Magnetic hysteresis of the nanorods at 300 K and 10 K.

respectively, in agreement with bulk crystallographic data for hematite[35]. Clear basal plane facets [100]/[010] and oblique facets [102] are evident at the serrated edges (Figure 2 d). The crystallinity of the nanoparticle appears within one or two monolayers from the surface, and there is no evidence of an amorphous shell. The electron loss spectroscopy (EELS) data detected at the centre, top and edges of the nanorod, as labelled in the inset, are consistent with the standard Fe^{3+} L-edge spectra, and the surface and bulk spectra show no obvious chemical shift within 0.1 eV.

The X-ray diffraction pattern of the α-Fe_2O_3 nanorods (Figure 3 ba) indicates that the chemical structure has the same space group and atomic positions as bulk α-Fe_2O_3, and the lattice constants are within 0.1 % of bulk α-Fe_2O_3. This agrees with past work which reported only subtle differences between nanorods, bulk, mesoporous hematite and nanocubes [25, 26]. Rietveld refinement was performed using the R-3c spacegroup in the hexagonic setting (R-3c: H) starting from the previously published structure of bulk Fe_2O_3 data taken from the Inorganic Crystal Structure Database, originally published in Ref [35]. The refinement gave reliability factor R_{wp}/R_{exp} = 1.62. The determined room temperature lattice constants were a = 5.031(1) Å and c= 13.792 Å. Both values are within 0.14% of the published crystal structure data (a = 5.038, c = 13.772). Similar results have been reported previously for nanorods[16, 26].

The low field magnetization versus temperature data (Figure 3 b) are relatively flat, with no sharp transitions in the nanorods between 300 K and 0 K. This indicates that the Morin transition is absent. At very high fields of 50 kOe, a spin-flop transition is observed at ~ 100 K (Figure 3 b), however, the magnetic moment increases at low temperature, unlike bulk Fe_2O_3. The magnetic hysteresis loops (Fig. 3 c) show a canted weak ferromagnetic hysterisis at 10 K and 300 K. This is further evidence for a suppressed Morin temperature because below the SR transition a linear dependency is expected in bulk hematite. It is is important to note that the magnetometry is only sensitive to the canted moment and not the antiferromagnetic sub-lattices themselves, and can, therefore, hide considerable complexity.

Unlike magnetometry, neutron diffraction is directly sensitive to the antiferromagnetic order parameter. The neutron diffraction patterns at various temperatures, taken from the elastic window (E = 0, Δ E = 0.2 eV in the TOF data) are plotted in Figure 4 a), b) along with simulated data in Fig. 4 c). Three peaks are observed and can be indexed as the (003), (101) and (102) of α-Fe_2O_3 using the hexagonal cell parameters. As the (003) and (101) diffraction peaks occur at structurally forbidden scattering conditions, they are entirely magnetic in origin and provide solid evidence that magnetic order is present in the nanorods at room temperature. An identical set of magnetic peaks have been detected in the nanoparticle, mesoporous and bulk α-Fe_2O_3 via powder neutron diffraction [24, 25]. The nanoparticle powder pattern is compared with bulk hematite powder (Figure 4 b) and the theoretically calculated intensities for the magnetic structures of bulk α-Fe_2O_3 in the true antiferromagnetic (AFM) and canted antiferromagnetic state (WFM) phase (Figure 4 c). At room temperature, both the bulk and nanopowder have similar magnetic structures evident in the magnetic Bragg diffraction peaks, however, at a lower temperature, the magnetic structures are significantly different. Whereas the bulk sample undergoes the Morin transition at T_{SR}~ 250 K, the spin structure of the nanorods remains trapped in the WFM state even to 1.5 K and consequently the low temperature and high temperature diffraction patterns are identical. The data Q-range is inadequate to perform a full Rietveld refinement,

however, it contains sufficient information to clarify the magnetic structure in the nanorods, based on comparison with the known bulk case. It is well-known that the magnetic intensity of elastic scattering for unpolarized neutrons is related to the square of the form factor F_M which depends on the spin component perpendicular to the neutron scattering vector [36]:

$$\boldsymbol{F_M(G_M)} = \sum \boldsymbol{p_j S_\perp e^{-iG_M \cdot d_j} e^{W_j}} \qquad (3)$$

where $\mathbf{G}_M$ is the reciprocal scattering vector, $\mathbf{S}_\perp$ is the spin magnetic component perpendicular to $\mathbf{G}_M$, p_j is the density of ion j, $\mathbf{d_j}$ encodes the real space position of the magnetic ions, and W_j describes a Debye-Waller factor. Consequently, the presence of the (003) peak indicates a large magnetic moment perpendicular to the *c*-direction, in the (110)/(-110) basal plane as expected for the so-called weak ferromagnetic structure. The strong (003) peak is observed in both the bulk and nanostructures at room temperature, leading to the assignment of the structure shown in Figure 3d which is the so-called weak ferromagnetic (WFM) state. As the canting in α-Fe_2O_3 is small (0.065 degrees), it is difficult to observe directly, and is inferred instead from magnetometry measurements. Below 250 K, the diffraction pattern changes strongly for the standard bulk SR, as expected due to the Morin transition. The (003) peak vanishes and the (101) peak increases in magnitude. As the (101) peak is partially sensitive to components of the magnetic moments along the *c*-direction, this implies that the magnetic moments in the bulk α-Fe_2O_3 have reoriented to yield a greater projection along (001), consistent with the low-temperature AF structure illustrated in Figure 3 e. In direct contrast, this feature never occurs in the nanostructured α-Fe_2O_3 sample and the (003) peak remains strong down to 2 K indicating that the α-Fe_2O_3 rods remain trapped in the high temperature magnetic structure with the spins in the *ab* plane. Previous magnetometry measurements on similar rods had also inferred the absence of a reorientation [26], however, the neutron diffraction directly confirms the details of the overall antiferromagnetic structure. Lastly, finite size is known to broaden peaks in nanostructures according to the Scherrer formula. On the other hand, given the relatively large sizes of the particles (*d*=60/300 nm), no broadening can be detected in the neutron diffraction within the instrumental peak resolution (FWHM =0.88±0.02°).

Despite the reduced dimensionality, the nanorod sample shows clear evidence of magnon excitations (Figure 5 a). These can be compared with the known spectrum of bulk α-Fe_2O_3 in its two magnetic structures (Figure 5 b,c) and with model spin-wave calculations (Figure 5 d) based on the model described in a later section. Due to the kinematic constraints on the neutron experiment, certain *Q/E* regions are inaccessible and these are indicated by the black masked

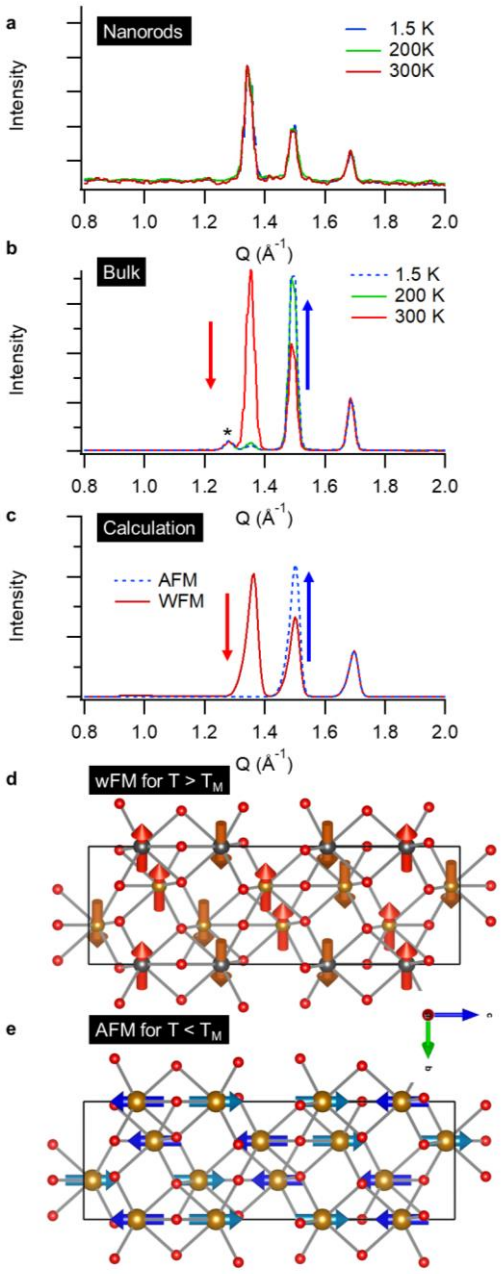

Figure 4. a) Low-angle neutron diffraction (ND) patterns of the nanorod sample indicate a constant magnetic structure over the temperature range between 1.5 – 300 K. b) ND patterns of the bulk α-Fe_2O_3 sample demonstrate the standard spin-reorientation effect that causes the intensity of the 101 and 003 peak to be modified. The * marks a small unknown impurity in the bulk sample. c) Simulated magnetic Bragg intensities for the weak ferromagnetic and antiferromagnetic structure. d) The magnetic structure of the weak-ferromagnetic structure superimposed on the chemical unit cell e) the magnetic structure of the AFM state.

regions. The inelastic data for the bulk and nanostructured material was subjected to the identical data treatment, and the same sample holders and instrument setup were used in each case so that the data are directly comparable. In all of the data, three main magnon dispersive features are observed within the measurable region at Q=1.31, 1.5 and 2.8 Å^{-1}, corresponding to magnetic points in the Brillouin zone. The signal for the nanorods is observable above background, however, owing to limited available mass for this sample, the error bar is larger and background noise plays a more noticeable role. Owing to the strong exchange constants, the two lower Q features (labelled *i*/*ii*) exhibit a very steep dispersion and the modes appear therefore as vertical lines on this energy scale, consistent with the past time-of-flight spectroscopy measurements [24]. This is equally true in the nanorod data. Consequently, the exchange parameters of the Hamiltonian must be very similar in the bulk and α-Fe_2O_3 nanorod, which would be expected given the similar Fe-O-Fe super-exchange

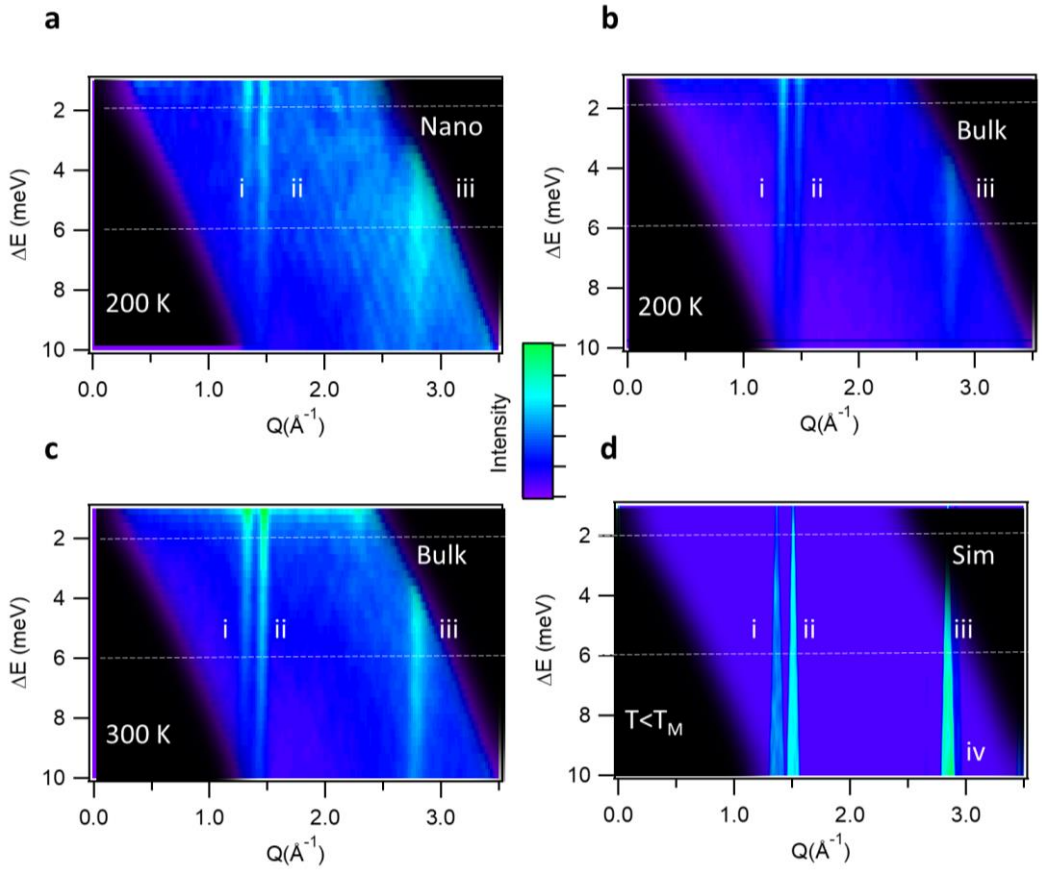

Figure 5. a) Time-of-flight inelastic neutron spectroscopy of the nanorod sample α-Fe_2O_3 at 200 K after background correction and normalization. b) INS for the control sample, bulk α-Fe_2O_3, in the AFM phase at 200 K. c) Neutron spectroscopy of the bulk α-Fe_2O_3 at 300 K. d) Powder-averaged, angular-averaged simulation of the magnon signal in the WFM of α-Fe_2O_3 using the model Hamiltonian parameters described in the text. Various features have been labelled i-iv) to facilitate comparison.

structure in both systems. On the other hand, it is apparent that the nanoparticle sample at 200 K exhibits significant differences from the 200 K bulk data in that features labelled *i* and *ii* have modified spectral intensities. Interestingly, the nanorod spectral intensities at 200 K (Figure 5 a) resemble the 300 K bulk data (Figure 5 c). This is expected, given that the 300 K bulk data and 200 K nanorod data share the same magnetic structure. Figure 5 d) shows the theoretically calculated spin-wave signal for a powder-averaged dispersion for the WFM phase of α-Fe_2O_3 using the parameters to be described in the later sections. Clearly, the model correctly produces the *Q*-values, dispersive character and relative intensity of the features *i* and *ii*. The primary difference between the calculated and measured spectrum is the broadening of the experimental data which also reduces the intensity of certain peaks. Although the instrumental resolution function produces broadening, the differences between the bulk and nanostructured experimental data must be intrinsic because the instrumental setup is identical.

To quantify the differences in the nanorod, constant energy cuts through the bulk and nanorod data for the 200 K are shown in Figure 6. The features were fitted to four Gaussian peaks on a linear background. The modified spectral intensity for the bulk and nanostructured material at 200 K is clear at features *i* and *ii*) in Figure 6 and b). Based on the calculations, this difference is simply a reflection of the different spin orientation, and consequently correctly reproduced by the model for the WFM and AFM states respectively, as shown in the line profile below the experimental data. A non-trivial difference in the experiment is the considerable additional broadening of the modes in the nanorod that is apparent at higher energy transfer (E = 6 meV) resulting in much weaker peak intensities for features labelled *i,ii, iii* in the nanorod data. The excess broadening of the nanostructured sample's full-width-at-half-maximum is between 5 and 20% relative to the bulk sample at 6 meV. Another notable difference is the appearance of a doublet feature labelled *iv* just above feature iii) in the nanorod data which is not apparent in the bulk data. Comparisons with the SpinW calculation indicate that a weak magnon branch is expected at *vi*, however, this feature appears to be distinct in the nanorods whereas it is blurred together with the stronger feature *iii* in the bulk data.

It is also useful to compare the data in the same magnetic structure, albeit at different temperatures. Figure 6 c) and d) therefore show the same line profiles for the bulk data at 300 K compared with the nanorod data at 200 K. In this comparison, the spectra for low energy transfer (E = 2 meV) virtually collapse of top of each other, and the relative intensity of features *i* and *ii* are the same. Only moderate broadening is noted in the nanorod sample in the low energy

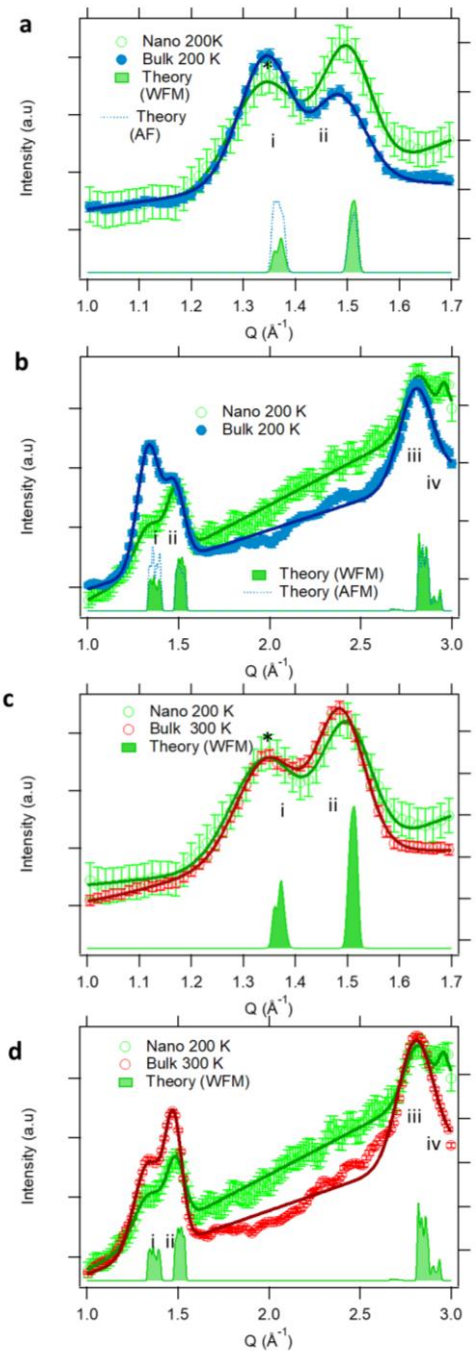

Figure 6. a) The constant *E*-cuts at E = 2 meV through the inelastic neutron spectra show a modified intensity for the bulk and nanorod α-Fe_2O_3 at 200 K b) Constant energy cut at E = 6 meV at 200 K c) Constant *E*-slice at E = 2 meV comparing the 200 K nanorod data with the 300 K bulk sample. d) Constant *E*-slice at E = 6 meV comparing the 200 K nanorod data with the 300 K bulk sample. The main features are labelled i-iv. Shaded lines are from the theoretical spinwave calculation.

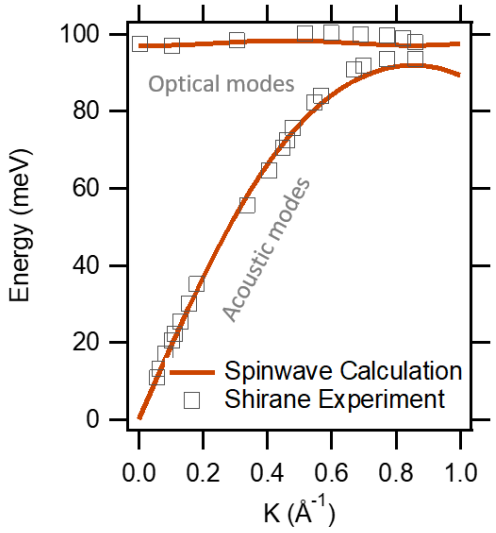

Figure 7. The model Hamiltonian proposed by Shirane correctly predicts the energy of acoustic and optical modes of bulk α-Fe_2O_3 as measured by their neutron spectroscopy using the new exchange constants derived in this work. High energy neutron data taken from and Samuelson and Shirane's measurements (1970).

region at 2 meV. On the other hand, at higher energy transfer (*E*=6 meV), the nanorod sample shows an additional broad feature at high *Q* and weaker overall intensity.

In order to understand the magnetic excitations, linear spin-wave theory was used to model the magnon dispersion of the bulk and nanostructured α-Fe_2O_3. This was followed by powder averaging, and shown previously in Figure 5 d, in order to facilitate comparison with the experiment. As a starting model, we adopt the 'textbook' exchange constants first published by Shirane and Samuelson derived by neutron spectroscopy of single crystals [33]. In this so-called S&S model, the exchange constants for superexchange logically follow from the Fe-O-Fe distances and bond-angles (i.e. the Goodenough-Kanamori rules). Table I reports the bond-length and relevant Fe-O-Fe bond angle for the four nearest neighbours, along with the exchange constant ratios as reported by Samuelson and Shirane. An interesting feature of the magnetochemistry in α-Fe_2O_3 is that the nearest neighbour Fe atoms are bonded with a high Fe-O-Fe bond angle, and consequently they have a weak ferromagnetic magnetic exchange. In contrast, the strongest interactions occur via the Fe-O-Fe bonds enhanced via antiferromagnetic super-exchange, which depends on how close the bond-angle is to 180 degrees. These correspond to the third and fourth nearest neighbours. Figure 7 shows the high energy triple-axis data (taken from the previous publication by Shirane [33]), compared with the calculated spin-wave dispersion using the values of J_1, J_2, J_3 and J_4 in the table. It is clear both the acoustic and optical modes are well-reproduced by this model. From the derivative of the dispersion, the group velocity for acoustic magnons around the dispersion points is in the range of 3 - 4.7 km/s. The bracketed numbers in Table I are the ratios of J_i/J_3 which define the overall features of the dispersion in natural units (i.e. up to a constant energy scaling factor). It is clear that the ratios are identical in the S&S model and the present work, however, the absolute energy scale differs by precisely a factor of two. It is important to note that the absolute value of J_i implicitly depends on the definition of the Hamiltonian. The Hamiltonian employed in the older work is formally different from the standard modern variant in this work [36] because it contains more double-counted terms in the expansion. It is important to consider this because the S&S values are still widely propagated in textbooks without reference to the precise Hamiltonian [1]. The primary exchange constants from our work are ~ 4 – 5 meV and are therefore entirely constituent with the high Neel temperature (960 K) and with the exchange constants found in other structurally related Fe^{3+} superexchange systems [37] [38] within the standard modern formalism. In contrast, the numbers in the S&S model are much too low if used in conjunction with Equation 1. Using the modern model, the *Q*-positions and relative intensity of all of the main features in the powder-averaged data are well reproduced. However, the line-broadening in the nanorods requires further explanation.

Table I. Exchange constants used in the model Hamiltonian. The exchange parameters are reported in meV, and the bracketed values are the ratios J_i/J_3.

Neighbour	Fe-Fe distance	Fe-O-Fe angle [degrees]	Exchange Parameters (This work)
1	2.9 Å	86.5.2	J_1=-1.03 meV (0.2)
2	2.971 Å	93.92	J_2=-0.28 meV (0.05)
3	3.364 Å	119.66	J_3=5.12 meV (1)
4	3.705 Å	131.58	J_4=4 meV (0.78)

It is remarkable that the diffraction peaks in the elastic channel of nanorod data are not broadened whereas the inelastic spectra at high energy transfer are. There are two possibilities that could explain this: 1) strong magnon scattering due to confinement at interfaces 2) dispersion broadening due to disorder in the exchange constants. Figure 7 shows

schematically the physical picture, along with the manifestation in the simulated spin-wave spectrum. Firstly, it is well known that finite-magnon lifetime can lead to an energy broadening of the lines in the energy dimension, where the quasiparticle lifetime is inversely related to the broadening. We show below, that in special cases, that effect can also be related to an effective broadening in *Q*. Multiple factors can reduce the magnon lifetime including three magnon scattering, and boundary scattering. Given the high group velocity of the magnons in hematite, they are expected to reach the boundary of the Fe_2O_3 rods within only 1.5 picoseconds, and boundary scattering may be important. An estimate of the energy broadening for magnons scattering at boundaries is given by the expression [39]:

$$\boldsymbol{\Gamma} = \hbar \frac{2v}{L} \qquad (4)$$

where v is the magnon group velocity, and L is the confinement length-scale from a boundary, interface or surface. It is important to note that this formula intrinsically assumes that the scattering of magnon occurs by a diffuse off-specular inelastic process. Using the shorter dimension of the nanorods (L = 60 nm) and the group velocities derived in the previous section, the upper limit on the broadening will be 2 meV. This could increase considerably to 16 meV for smaller domains at the 5 nm scale. This meV-scale broadening is three orders of magnitude larger than the lifetime broadening observed in 3D antiferromagnets with large crystallites[39]. Neverthless, given the strong 'vertical' nature of the spin-wave dispersion in α-Fe_2O_3 in the experiment, time-of-flight powder spectroscopy is ill-suited to observe the broadening in *E*, and the main effects of the broadening in energy will manifest instead as small effective *Q*-broadening by causing smearing of intensity between different energy windows of the dispersion. Simulations incorporating variable levels of energy broadening in the pattern are shown in Fig 8 b-c), along with their line profiles based on constant-energy *E*-slices at 2 and 6 meV through the model. While this model does produce a broadening in *Q* that should be observable in future nanoparticle experiments, the effect is subtle for hematite even for ultra-short magnon lifetimes. Furthermore, the effective *Q*-broadening has the most noticeable effect at low energy in contrast to experiment. If the group velocity of the magnon is modified strongly at different points on the dispersion then this could produce different levels of broadening, however, this is unlikely in α-Fe_2O_3 since the low energy scale is dominated by acoustic modes.

An alternate mechanism that can lead to *Q*-broadening of the feature is the presence of a disorder that leads to a distribution of values in the exchange network ($J_n \rightarrow J_n'$) or the local spin moments (S→S'). This is feasible given that nanoparticles generally exhibit increased structural disorder, which may manifest as a distribution of Fe-O-Fe bond angles which modulate J_n around the average values represented in Table I. Furthermore, even if the nano α-Fe_2O_3 particles were structurally perfect, the proximity to surfaces invariably decreases the local spin moment (S' < S) according to Monte Carlo results [40]. Assuming constant scaling of all constants such that $J_N' = J' J_N$, the dispersion depends on both J' and S' in the Hamiltonian, and so either would lead to an equivalent modified magnon band structure. Figure 8 b) shows the broadening for various values of J' modified from bulk α-Fe_2O_3. Clearly reducing J' by 10% or more leads to strong broadening of the modes in the energy range. In agreement with experiment, the broadening is largest at higher energy transfers. It appears that a distribution of exchange constants with all components reduced by only 10-20% from the bulk α-

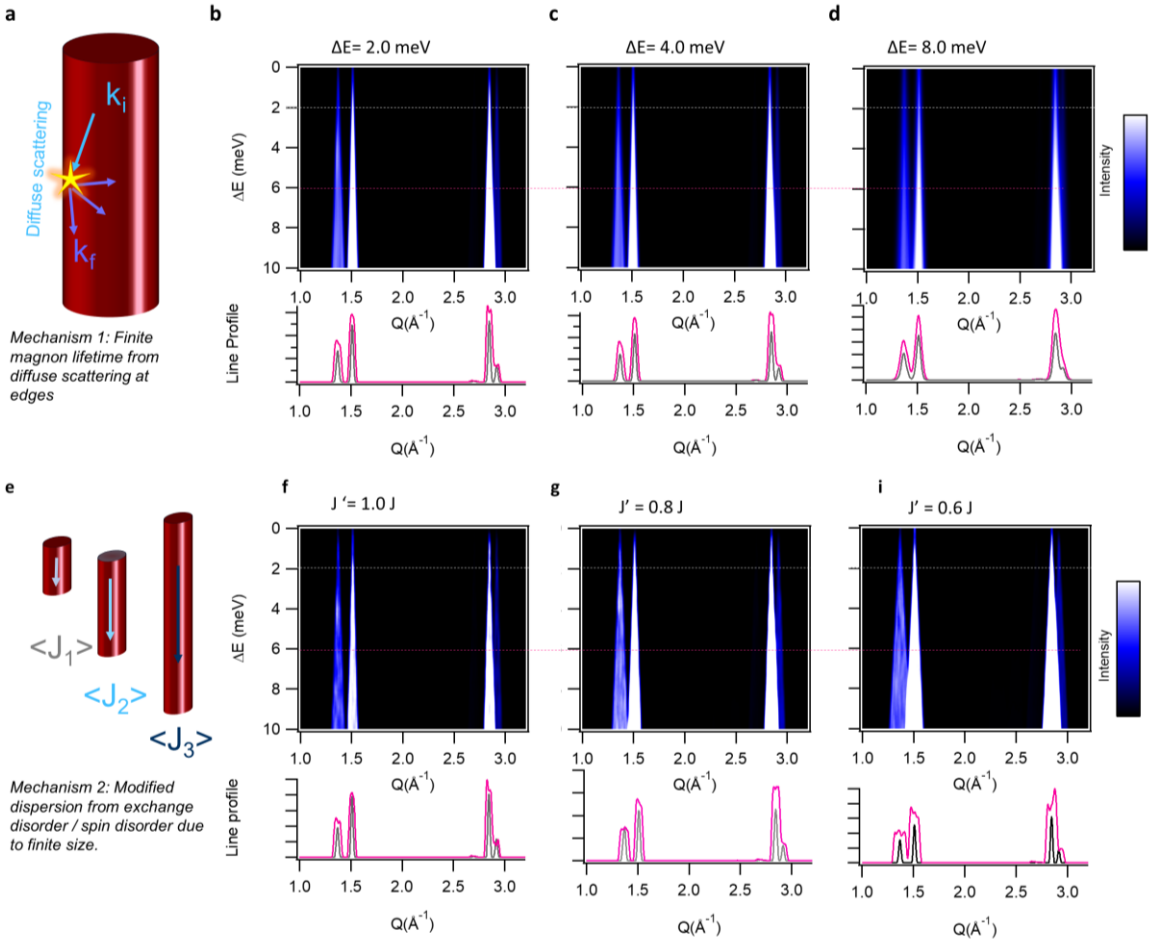

Figure 8. a) Rapid magnon scattering from collisions with the rod edge can lead to energy-broadening of the magnon bands from finite-life time. b-d) Energy broadening manifests as smearing of intensity from high energy transfer to low energy transfer which yields an effective *Q*-broadening and a Lorentzian line-shape in *q* as shown in the line profiles. b) A second mechanism that can lead to effective *Q*-broadening is a modified dispersion caused by modified exchange-bond network (J') or, equivalently, a reduced local spin moment (S). This causes strongest broadening at high energy transfer, and leads to a flat-top line shape and additional multi-peak features at higher energy transfer.

Fe_2O_3 exchange constants is sufficient to cause the level of broadening observed in the experimental study. Furthermore, the effect of energy smearing from finite magnon lifetime leads to a broader Lorentzian shape for peaks in a constant *E*-slice, whereas the effect of lower J'S' values leads to a flat-top line shape caused by as the spread of several features in the dispersion increases. This scenario may explain the enhanced contrast of feature *iv* observed at high energy transfer in the nanorod experiment (Figure 5 a).

4. Conclusion

The direct observation of long-range magnons propagating with a diameter of 60 nm is promising for the development of possible future magnonic devices based on nanowires. This Article also provides further fundamental evidence of a shape dependency in the Morin transition in α-Fe_2O_3 nanoparticles. It is clear that simply applying the finite-size scaling argument from spherical particles does not explain the observations in the nanorods.~~,~~ For example, for large spherical particles with an equivalent diameter to the rods in this work (*d*= 60 nm), one would predict T_{SR} = 212 K using Equation 1 in agreement with experiments on spherical particles [18]. However, if the minimum finite length-scale were the only relevant parameter,

one would expect a similar T_{SR} in the nanorods. In contrast, we find that T_{SR} is suppressed in the nanorods(T_{SR} < 1. 5 K) clearly indicating that particle shape and surface facetting both play a decisive role. An interesting consequence of this is that hysteretic properties and the magnon propagation in Fe_2O_3 nanorods are governed by the weak ferromagnetic structure down to at least 1.5 K . Furthermore, the spectrum overall is very close to that of bulk hematite in the weak ferromagnetic phase, indicating that a strongly modified spin-wave spectrum is not a necessary prequisite for a modified spin reorientation behavior. Our results indicate that the low-energy parts of the Hamiltonian (eg. the anisotropy and DM interaction modified by surface effects) are the best candidates to explain the modified spin-reorientation in the nanorod α-Fe_2O_3 because the higher-energy exchange terms are very similar, to within a few percent, of the bulk values. An unexpected, but consequential finding of this paper is that it is we have rederived the textbook exchange constants for α-Fe_2O_3 using the modern, standardized form of the Hamiltonian. These are two times the often-quoted values presented by Samuelson and Shirane owing to the subtly different form of Hamiltonian used in their original work [33]. Using extensive spin-wave modelling, we have proposed two general mechanisms that could account for broadening in the nanoparticle magnon modes: disorder in exchange constants, and extreme lifetime broadening from finite-size constraints. Future inelastic neutron studies using highly monodisperse nanosamples of various sizes should be able to disentangle these effecst. Until then, despite being one of the oldest known antiferromagnets, it appears that α-Fe_2O_3 still holds some unresolved mysteries.

Acknowledgements

D.L.C thanks Professor Roger Lewis and Prof. Garry McIntyre for valuable discussions. This research was partially supported by the Australian Research Council Centre of Excellence in Future Low-Energy Electronics Technologies (project number CE170100039 and funded by the Australian Government. The authors are grateful for access to neutron beam-time (P5345) granted by the Australian Nuclear Science and Technology Organisation. X. L. Wang acknowledge the support of an ARC Future Fellowship.

Appendix A

To quanitfy the possible effect of the Dzyaloshinskii-Moriya and anisotropy on the spin wave spectrum, additional calculations were performed with the expanded Hamiltonian:

$$\mathcal{H} = \sum_{i,j} \boldsymbol{S_i J_{ij} S_j} + \sum_{i,j} \boldsymbol{D_{ij}}.\boldsymbol{S_i} \times \boldsymbol{S_j} + \sum_i \boldsymbol{S_i K_i S_i}$$

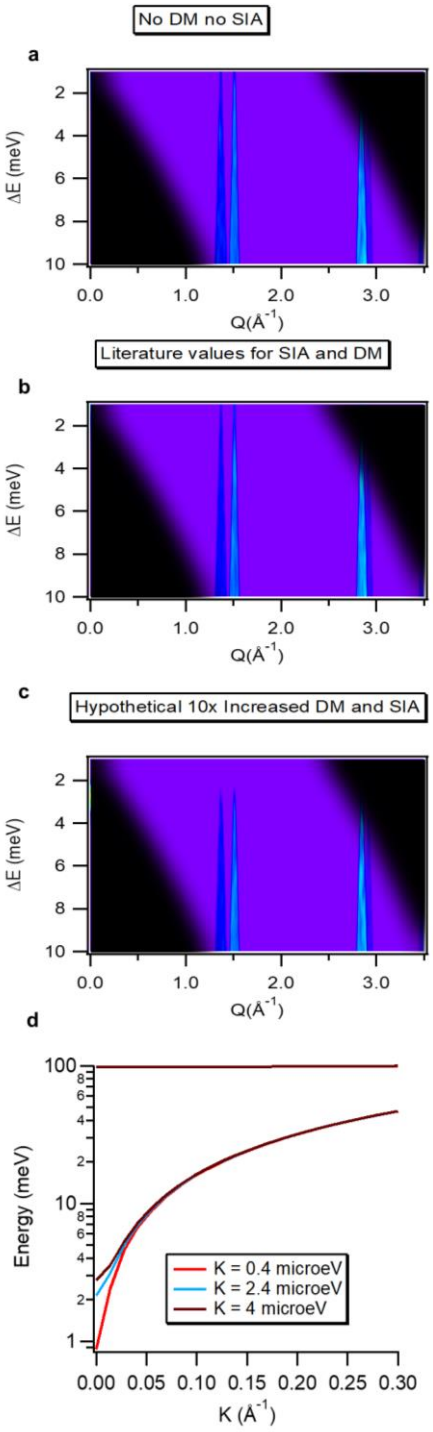

Figure 9 (Appendix). a) Powder-averaged simulated spectrum for *D*=0, K=0. b) Simulated spectrum for *D*= 12 μeV and K = 0.4 μeV. c) Simulated spectrum for *D*= 120 μeV and K = 4 μeV. d) Simulated magnon dispersion curves along the (~~001~~111) direction for different values of K.

where $\mathbf{K_i}$ was orientated along (-1,-1,2) to model an easy plane axis in the basal plane with magnitude K, and the microscopic D_{ij} vectors were selected to obey the required symmetry restrictions, whilst producing a net component along (0001) with magnitude *D*. As K and *D* are extremely small in Fe_2O_3 (3 orders of magnitude smaller than J_{ij}), their precise values and orientations are only approximately known [1, 23]. In Figure 9 a) simulations with K and *D* = 0, matching those in the text. In Figure 9 b) estimated values of K=0.4 μeV and *D* =12 μeV are taken from the literature [1], and there is no observable difference with Fig. 9 a because the differences are too small to observe. Figure 9 c shows that these values would need to be increased at least ten fold to produce an observable spin-gap in this energy range. Figure 9 d shows the magnon dispersion for different values of K.

About the author

David Cortie obtained his PhD from the University of Wollongong, Australia in 2013 focussing on neutron scattering in magnetic nanostructures. He subsequently took up a Fellowship at the University of British Columbia at Quantum Matter Centre jointly affiliated Max-Planck Institute for Quantum Matter. There he worked on applying β-NMR, a technique closely related to μSR, to strongly correlated oxide magnetic materials. In 2016, he transferred to a post-doctoral position at Australian National University / Australian Nuclear Science and Technology Organisation utilizing *ab initio* calculations and molecular dynamics to study the structure-function relationship in transition metal oxides. In 2018 he was awarded a Discovery Early Career Research Award based at the University of Wollongong examining magnetic proximity effects between topological insulators and strongly-ordered magnetic materials.

References

[1] Morish A H 1994. *Canted antiferromagnetism : hematite*: Singapore : World Scientific)

[2] Cortie D L, Lin K W, Shueh C, Hsu H F, Wang X L, James M, Fritzsche H, Brück S and Klose F 2012 Exchange bias in a nanocrystalline hematite/permalloy thin film investigated with polarized neutron reflectometry *Phys. Rev. B* **86** 054408

[3] Dho J, Leung C W, Barber Z H and Blamire M G 2005 Controlling the exchange interaction using the spin-flip transition of antiferromagnetic spins in $Ni_{81}Fe_{19}$/α-Fe_2O_3 *Journal of Applied Physics* **97** 10K101

[4] Bae S, Judy J H, Fenner D B, Hautala J, Egelhoff W F, Chen P J and Gan L 2008 Effects of gas-cluster ion beam processing on physical, magnetic, and giant magnetoresistance properties of α-Fe_2O_3 bottom spin-valves *Journal of Magnetism and Magnetic Materials* **320** 2001-9

[5] Lebrun R, Ross A, Bender S A, Qaiumzadeh A, Baldrati L, Cramer J, Brataas A and Kläui M 2018 https://arxiv.org/ftp/arxiv/papers/1805/1805.02451.pdf

[6] Chumak A V, Serga A A and Hillebrands B 2014 Magnon transistor for all-magnon data processing *Nature Communications* **5** 4700

[7] Liang Q-F, Zhou J, Yu R, Wang X and Weng H 2017 Interaction-driven quantum anomalous Hall effect in halogenated hematite nanosheets *Phys. Rev. B* **96** 205412

[8] Özdemir Ö, Dunlop D J and Berquó T S 2008 Morin transition in hematite: Size dependence and thermal hysteresis *Geochemistry, Geophysics, Geosystems* **9** 1-12

[9] Dang M Z, Rancourt D G, Dutrizac J E, Lamarche G and Provencher R 1998 Interplay of surface conditions, particle size, stoichiometry, cell parameters, and magnetism in synthetic hematite-like materials *Hyperfine Interactions* **117** 271-319

[10] Schroeer D and Nininger R C 1967 Morin Transition in a-Fe_2O_3 Microcrystals *Phys. Rev. Lett.* **19** 632-4

[11] Gallagher P K and Gyorgy E M 1969 Morin Transition and Lattice Spacing of Hematite as a Function of Particle Size *Physical Review* **180** 622-3

[12] Krinchik G S and Zubov V E 1975 Surface magnetism of hematite *Zh. Eksp. Teor. Fiz* **69** 707-21

[13] McEnroe S A, Carter-Stiglitz B, Harrison R J, Robinson P, Fabian K and McCammon C 2007 Magnetic exchange bias of more than 1 Tesla in a natural mineral intergrowth *Nature Nanotechnology* **2** 631

[14] Li L, Li F, Wang J and Zhao G 2014 Finite-size scaling law of the Néel temperature in hematite nanostructures *Journal of Applied Physics* **116** 174301

[15] Shinjo T, Kiyama M, Sugita N, Watanabe K and Takada T 1983 Surface magnetism of α-Fe_2O_3 by Mössbauer spectroscopy *Journal of Magnetism and Magnetic Materials* **35** 133-5

[16] Chen Y H and Lin C C 2014 Effect of nano-hematite morphology on photocatalytic activity *Physics and Chemistry of Minerals* **41** 727-36

[17] Zysler R D, Fiorani D, Testa A M, Godinho M, Agostinelli E and Suber L 2004 Size effects in the spin–flop transition of hematite nanoparticles *Journal of Magnetism and Magnetic Materials* **272-276** 1575-6

[18] Xu S, Habib A H, Gee S H, Hong Y K and McHenry M E 2015 Spin orientation, structure, morphology,

and magnetic properties of hematite nanoparticles *Journal of Applied Physics* **117** 17A315

[19] Bødker F, Hansen M F, Koch C B, Lefmann K and Mørup S 2000 Magnetic properties of hematite nanoparticles *Phys. Rev. B* **61** 6826-38

[20] Cortie D L, Buck T, Dehn M H, Karner V L, Kiefl R F, Levy C D P, McFadden R M L, Morris G D, McKenzie I, Pearson M R, Wang X L and MacFarlane W A 2016 β-NMR Investigation of the Depth-Dependent Magnetic Properties of an Antiferromagnetic Surface *Phys. Rev. Lett.* **116** 106103

[21] Klausen S N, Lefmann K, Lindgård P A, Clausen K N, Hansen M F, Bødker F, Mørup S and Telling M 2003 An inelastic neutron scattering study of hematite nanoparticles *Journal of Magnetism and Magnetic Materials* **266** 68-78

[22] Hansen M F, Bødker F, Mørup S, Lefmann K, Clausen K N and Lindgård P-A 1997 Dynamics of Magnetic Nanoparticles Studied by Neutron Scattering *Phys. Rev. Lett.* **79** 4910-3

[23] Chow H and Keffer F 1974 Soft surface magnons and the first-order magnetic phase transitions in antiferromagnetic hematite *Phys. Rev. B* **10** 243-54

[24] Hill A H, Jacobsen H, Stewart J R, Jiao F, Jensen N P, Holm S L, Mutka H, Seydel T, Harrison A and Lefmann K 2014 Magnetic properties of nano-scale hematite, α-Fe_2O_3 studied by time-of-flight inelastic neutron spectroscopy *The Journal of Chemical Physics* **140** 044709

[25] Hill A H, Jiao F, Bruce P G, Harrison A, Kockelmann W and Ritter C 2008 Neutron Diffraction Study of Mesoporous and Bulk Hematite, α-Fe_2O_3 *Chem. Mater.* **20** 4891-9

[26] Wang J, Aguilar V, Li L, Li F-g, Wang W and Zhao G 2015 Strong shape-dependence of Morin transition in α-Fe_2O_3 single-crystalline nanostructures *Nano Research* **8** 1906-16

[27] Kamzin A S and Vcherashnii D B 2002 Spin-reorientation phase transition on the surface and in the bulk of α-Fe2O3 single crystals *Journal of Experimental and Theoretical Physics Letters* **75** 575-8

[28] Nikolov O, Ruskov T, Tomov T and Toshev A 1988 A Mössbauer study of the Morin transition on the surface and in the bulk of hematite single crystals *Hyperfine Interactions* **39** 409-17

[29] Rodríguez-Carvajal J 1993 Recent advances in magnetic structure determination by neutron powder diffraction *Physica B: Condensed Matter* **192** 55-69

[30] Yu D H, Mole R, Noakes T, Kennedy S and Robinson R 2013 PELICAN - a Time of Flight Cold Neutron Polarization Analysis Spectrometer at OPAL *J. Phys. Soc. Jpn.* **82**

[31] Richard D, Ferrand M and Kearley G J 1996 Analysis and visualisation of neutron-scattering data *J. Neut. Res.* **4** 33-9

[32] Toth S and Lake B 2015 Linear spin wave theory for single-Q incommensurate magnetic structures *Journal of Physics: Condensed Matter* **27** 166002

[33] Samuelsen E J and Shirane G 1970 Inelastic neutron scattering investigation of spin waves and magnetic interactions in α-Fe_2O_3

physica status solidi (b) **42** 241-56

[34] Momma K and Izumi F 2011 VESTA 3 for three-dimensional visualization of crystal, volumetric and morphology data *J. Appl. Crystallogr.* **44** 1272-6

[35] Blake R L, Hessevick R E, Zoltai T and Finger L W 1966 Refinement of the hematite structure *American Mineralogist* **51** 123-9

[36] Shirane G, Shapiro S M and Tranquada J M 2002 *Neutron Scattering with a Triple-Axis Spectrometer: Basic Techniques* (Cambridge: Cambridge University Press)

[37] Matsuda M, Fishman R S, Hong T, Lee C H, Ushiyama T, Yanagisawa Y, Tomioka Y and Ito T 2012 Magnetic Dispersion and Anisotropy in Multiferroic $BiFeO_3$ *Phys. Rev. Lett.* **109** 067205

[38] Jeong J, Goremychkin E A, Guidi T, Nakajima K, Jeon G S, Kim S-A, Furukawa S, Kim Y B, Lee S, Kiryukhin V, Cheong S W and Park J-G 2012 Spin Wave Measurements over the Full Brillouin Zone of Multiferroic $BiFeO_3$ *Phys. Rev. Lett.* **108** 077202

[39] Bayrakci S P, Tennant D A, Leininger P, Keller T, Gibson M C R, Wilson S D, Birgeneau R J and Keimer B 2013 Lifetimes of Antiferromagnetic Magnons in Two and Three Dimensions: Experiment, Theory, and Numerics *Phys. Rev. Lett.* **111** 017204

[40] Binder K and Landau D P 1990 Critical phenomena at surfaces *Physica A: Statistical Mechanics and its Applications* **163** 17-30